Electrical Power and Energy Systems 155 (2024) 109561

Contents lists available at ScienceDirect

International Journal of Electrical Power and Energy Systems

journal homepage: www.elsevier.com/locate/ijepes

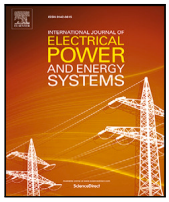

Determination of modular multilevel converters admittances and their impacts on HVDC power system stability

D. del Giudice [a], F. Bizzarri [a,b], D. Linaro [a], A. Brambilla [a,*]

[a] Dipartimento di Elettronica, Informazione e Bioingegneria, Politecnico di Milano, p.za Leonardo da Vinci, 32, I20133, Milano, Italy
[b] Advanced Research Center on Electronic Systems "E. De Castro" (ARCES), University of Bologna, Italy

ARTICLE INFO

Keywords:
Modular multilevel converters
periodic small-signal analysis
shooting method
Small-signal impedance/admittance model

ABSTRACT

This paper deals with the determination of the complex admittances and trans-admittances of power converters in general and in particular of two modular multilevel converters (MMCs) connected by a high-voltage direct current (HVDC) link to two distinct AC systems. With the term trans-admittances we mean the cross admittance "seen" between the points of common coupling of the two MMCs in the two AC grids. These quantities show how the HVDC link couples the two seemingly separated AC systems. The accurate computation of admittances and trans-admittances requires careful consideration of several frequency harmonics and frequency up-conversion/down-conversion phenomena through the HVDC link. To determine them, we exploit the periodic small-signal (PAC) analysis that we briefly introduce from a theoretical perspective. Results show how AC and DC instabilities can be induced by MMCs and how they propagate through the HVDC link.

1. Introduction

Modular multilevel converters have become the technology of choice in high-voltage direct current (HVDC) transmission systems thanks to their scalability to high voltages and powers, lower switching activity of the submodules (SMs) in their legs, higher waveform quality, and efficiency [1–5]. Nowadays MMC-based HVDC links are employed to efficiently connect separated (possibly asynchronous) AC networks or portions of the same AC grid, as well as remote energy production sites (e.g., wind farms) to the continental grid.

As the presence of these converters in electric power systems increases, so does their potential impact on the overall power system stability. Time domain simulations, despite being in principle a viable solution to investigate stability, would be unsuitable as they lead to a high computational burden. On the contrary, approaches based on small-signal analysis and eigenvalue analysis are preferred because they quickly provide adequate information about the stability characteristics of the power system under study.

A popular way of assessing the stability of a grid comprising converters consists in examining their impedances/admittances obtained with small-signal analysis [6]. However, the determination of MMC admittances is a complex task. Small-signal analysis approaches in conventional power grids without AC/DC converters rely on two main hypotheses: (i) all electrical quantities are characterized only by the positive sequence and (ii) harmonics are absent. Under these assumptions, the power flow (PF) solution corresponds to an equilibrium point in the DQ0-frame. Hence, power grids are modeled in the DQ0-frame and their models can be linearized around this *constant* PF solution, thus obtaining a *linear time-invariant* (LTI) system. Finally, the small-signal analysis can be performed by sweeping the frequency range in discrete steps over a given range (i.e., a version of the so-called *frequency scan* is executed), allowing the computation of specific admittances at each frequency.

In converter-based grids, this approach can still be applied if the assumptions above are still adequate. However, MMCs have a complex topology and control schemes that include, among others, inner and outer control loops, a PLL, a circulating current suppression strategy, and a capacitor voltage balancing algorithm [7,8]. These features result in highly non-linear, switching and decisional (digital) models of MMCs characterized by a multi-frequency response and non-negligible harmonics. Therefore, the Park transform applied to accurate three-phase models no longer leads to a *constant* PF solution but a *periodic solution* in the DQ0-frame. Consequently, the conventional computation of the PF is unfeasible and LTI small-signal models can no longer be used. To add even further to the challenge, perturbations in one AC network may interact with the MMC harmonics and be down-converted to frequencies close to the DC one. In turn, in the case of HVDC systems, they may propagate through the HVDC link and be up-converted by the MMC at the opposite end, which might then interact with its neighboring AC grid.

* Corresponding author.
E-mail addresses: davide.delgiudice@polimi.it (D. del Giudice), federico.bizzarri@polimi.it (F. Bizzarri), daniele.linaro@polimi.it (D. Linaro), angelo.brambilla@polimi.it (A. Brambilla).

https://doi.org/10.1016/j.ijepes.2023.109561
Received 13 June 2022; Received in revised form 30 May 2023; Accepted 7 October 2023
Available online 17 October 2023

The listed complexity and the impossibility to neglect harmonics have led to an abundance of *ad hoc* methods to derive MMCs impedances/admittances. One of the leading approaches consists in simplifying the MMC control scheme and grouping the SMs in each arm in simpler aggregates to obtain an overall model that, if recast in the DQ0-frame, still leads to an LTI model because harmonics are neglected [9,10]. Due to the assumptions introduced, however, this approach leads to a loss in accuracy.

Harmonics can still be taken into account by resorting to more sophisticated approaches [9,11,12]. For instance, recent papers proposed MMC formulations based on harmonic state space [11,13], which dates back to at least 2008 (see [14] and references therein), and dynamic phasors [15], which date back to 1999 [16]. In particular, in [15] the LTI small-signal model of a simplified version of an MMC, based on a single small-signal input tone and the derivation of the corresponding single output tone (SISO), is improved by exploiting the harmonic state-space modeling approach, thereby leading to a small-signal model that exploits multiple input tones and computes multiple output tones (MIMO).

The approaches adopted in all the cited papers (and several others in the literature) are *analytical*. Thus, they typically require cumbersome pen-and-paper derivations of the MMC harmonic state space (or dynamic phasor-based) model. To reduce the complexity of the analytical problem at hand, the MMC structure and control scheme are usually greatly simplified. This approach is not easily applicable when changes in the MMC configuration and controllers occur. Indeed, whenever changes are made, the analytical derivations need to be performed almost from scratch and may require different simplifications of the MMC model.

Contrary to the approaches described above, the paradigm we present is purely *numerical*. Our target is the derivation of impedances/admittances through simulations of potentially any converter configuration and among these of MMCs, which we consider in this paper. Our paradigm avoids any burdensome pen-and-paper analytical derivation or simplification of the MMC structure and controllers. Whenever changes occur in the system under study, the analysis must be simply run again to gather new results.

The method we present is known as periodic small-signal (PAC) analysis. It is a tool to perform small-signal stability analysis [17,18], that, as far as we know, has never before been used or implemented in power system simulators (even commercial ones) to study system stability. We present it by considering a completely general formulation that does not refer to a specific power system and converter topology. Indeed, contrary for example to harmonic state-space modeling, PAC formulation is in the *time domain*. This formulation is advantageous because it allows handling events such as threshold crossing and element switching in great detail, i.e., to efficiently deal with *hybrid* differential–algebraic equations [19].[1]

The PAC requires the execution of three steps, each of which relies on a distinct algorithm directly implemented at simulator level [20–22]. The first one computes the steady-state solution of the power system in the ABC-frame. The second one linearizes the model of the power system along the periodic orbit computed at the previous step, derives the monodromy matrix and the linear time-varying (LTV) model. Finally, the third algorithm performs a multiple-input/multiple-output frequency-domain analysis of the LTV model and derives the impedances/
admittances. Each single algorithm used in this process was already described in different contexts [23–25]. Here they are formulated and used in a coordinated and cooperative way to implement a novel approach for computing admittances of converters.

In addition to the advantages described above, the PAC method allows deriving an MMC admittance model that is richer than the canonical one, which is obtained by simplifying the MMC topology and control scheme so that the linearized circuit model is still LTI [9,10]. This is due to the fact that, when using PAC, the steady-state model of the MMC is linearized along a periodic orbit and not in the neighborhood of a stationary solution, thus leading to a small-signal periodic LTV circuit instead of a LTI one. These two classes of circuits react differently to small-signal disturbances. Indeed, injecting a sinusoidal signal into an LTI circuit will result in a steady-state response oscillating at the same frequency; on the other hand, applying the same sinusoid to a periodic LTV circuit causes the system to produce an output signal characterized by several frequencies (i.e., frequency up/down conversion phenomena are observed), which provide the user with more information than that inherent to the canonical one. This means that the admittance model derived through the PAC method allows predicting instability issues in cases in which the canonical impedance model would fail.

After presenting PAC analysis from a theoretical perspective, we apply it to derive some admittances and trans-admittances of the two MMCs of the Cigre DCS1 HVDC system. Results obtained with PAC analysis are validated by accurate transient stability analyses of the same HVDC system. In particular, we refer to *trans-admittances* as the admittances between the points of common coupling of two MMCs in two distinct AC grids. Starting from the computed admittances, we identify possible weak design aspects that could lead to instability in the AC and DC networks. Trans-admittances show how the HVDC link couples the two (seemingly separated) AC grids and how possible disturbances may propagate from one grid to the other and vice versa. Moreover, we show that in some cases frequency up/down conversion phenomena might affect system stability. To the best of the authors' knowledge, these are relevant aspects rarely described before due to the lack of simulation tools and difficulties in studying the stability of full-fledged MMC-based HVDC system with analytical approaches.

2. Admittance computation with the PAC analysis

2.1. MMCs *in a nutshell*

Fig. 1(a) depicts the typical structure of an MMC made up of three legs, each consisting of an upper and lower arm. Every arm comprises an RL filter and a cascading stack of up to several hundreds of identical SMs that can implement different topologies [4,5]. Their gate signals derive from a controller like that in Fig. 1(c), which includes four main sections.[2]

Section ① converts the voltages and currents at the MMC point of common coupling to direct and quadrature components in the positive sequence. A phase-locked loop (PLL) synchronizes the internal reference signals to the AC frequency. It tracks the grid frequency by regulating v_q^p to zero [26].

The outer power loop ② determines the reference DQ axis currents based on specific control objectives, such as active power control [27]. The inner current loop ③ computes the reference voltages at the **a**,**b**,**c** terminals necessary for the currents retrieved in ① to track their reference values obtained from ②. Through the inverse Park transform, the reference voltages are expressed in the ABC-frame [28].

MMCs require a scheme to limit circulating currents, which are caused by the voltage inequality among arms. Section ④ replicates the control scheme of Mathe [1] and Tu et al. [29], which outputs an additional reference voltage aimed at suppressing the double-line frequency negative sequence component of these currents.

Lastly, the reference voltages obtained in sections ③ and ④ are combined with the measured DC-side voltage to obtain the modulation indexes of the upper and lower arms of the MMC. If a detailed MMC model is adopted, these indexes correspond to specific gate signals, which

[1] In the frequency domain, handling of events in an accurate way will require a prohibitive number of harmonics.

[2] Some implementation details, which are omitted in this paper for the sake of brevity, can be found in the references listed in the following.

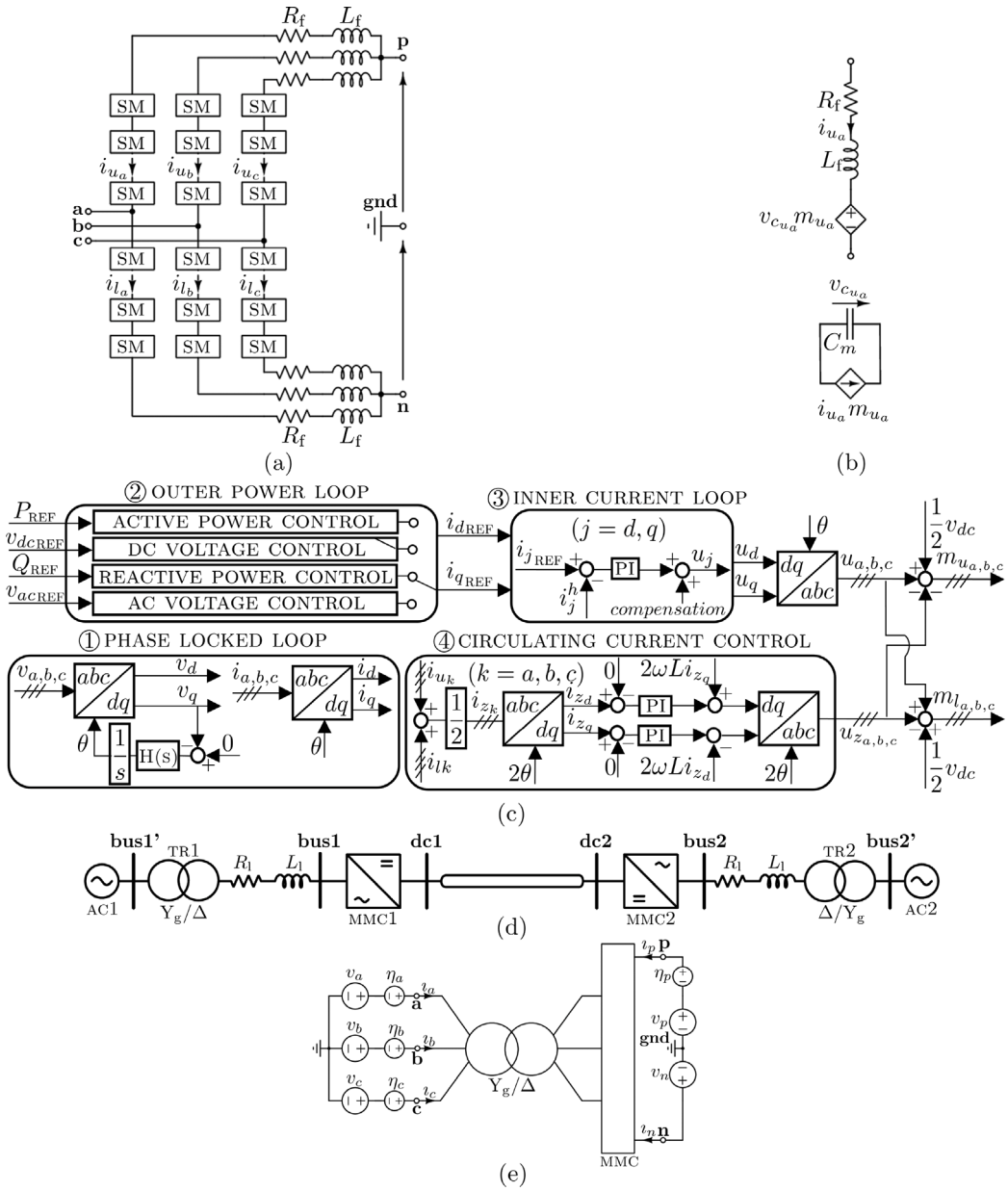

Fig. 1. (a) The high-level block schematic of the MMC model. (b) Generic arm representation in the MMC average model for phase-a, upper arm [30]. (c) MMC control scheme. (d) The schematic of the DCS1 HVDC test system described in [27]. (e) MMC representation as a 5-terminal component.

can be regulated through a capacitor voltage balancing strategy. In this paper, we resort to the average arm MMC model described in [30], shown in Fig. 1(b) for the upper MMC arm of phase-a. This equivalent model includes current and voltage dependent sources driven by the modulation indexes of the MMC arms, whose purpose is to mimic the behavior of the cascading stack of SMs in each arm.

2.2. The PAC analysis

We are now facing the problem of determining the admittances and trans-admittances of MMCs at their AC and DC ports. To do so, we resort to the PAC analysis [17,18]. This approach consists of three steps, which can be summarized as follows.

(i) the SHT method determines the periodic steady-state working conditions of the whole power system in the time domain, MMCs included, in the absence of small-signal perturbations [31,32];

(ii) the entire power system, including the MMCs, is linearized around its periodic steady-state solution in the time domain, thus leading to a periodic linear time-varying (LTV) small-signal model;

(iii) a small-signal perturbation is injected in this model and the resulting small-signal solution is computed. Admittances are derived accordingly.

Steps (i–iii) can be further detailed as follows:

(i) To introduce the SHT method, we consider the following generic semi-explicit index-1 differential–algebraic equations (DAEs) [33] with initial conditions at t_0 describing the dynamics of the entire power system

$$\begin{cases} \boldsymbol{\Lambda}\dfrac{d\boldsymbol{\xi}(t)}{dt} = \boldsymbol{F}(\boldsymbol{\xi}(t),\boldsymbol{\zeta}(t)) \\ \mathbf{0} = \boldsymbol{G}(\boldsymbol{\xi}(t),\boldsymbol{\zeta}(t)) \\ \boldsymbol{\xi}(t_0) = \boldsymbol{\xi}_0 \end{cases}, \tag{1}$$

where $\boldsymbol{\xi}(t) \in \mathbb{R}^N$ are the state variables, $\boldsymbol{\zeta}(t) \in \mathbb{R}^M$ are the algebraic variables, and $\boldsymbol{\Lambda} \in \mathbb{R}^{N\times N}$ is non-singular matrix.

It is worth highlighting that the equations in (1) can be automatically derived in simulation programs by several well known techniques, including the modified nodal analysis.[3] Starting from a netlist describing the whole system under study (MMC and its control scheme included), this analysis derives which variables in the system are state or algebraic variables and builds the matrices in (1), which are then exploited in steps (i–iii) of PAC. Both these steps and the modified nodal analysis are implemented in the software of the simulator used in this work (see[8]). Thus, they are carried out numerically, without needing to explicitly state the model of any part of the system, simplify them, and resort to pen-and-paper computations.

Starting from the $\boldsymbol{\xi}_0$ initial condition, (1) can be solved in the time domain to find the steady-state operation of the system. In principle, a brute force and sufficiently long lasting time-domain simulation would suffice to bring the entire power system (MMCS included) in (1) to (unperturbed) periodic steady-state operation [36,37]. Once this working condition is reached, it can be used to analyze system stability by considering different perturbation sets. However, this often leads to CPU-intensive and prohibitively time-consuming simulations.

The SHT method follows a different approach to find the periodic steady-state operation of (1). Indeed, it assumes that the $\boldsymbol{\xi}(t_0)$ initial condition is *unknown* and looks for a value such that, after the T_s working period corresponding to $1/f_s$ (e.g., 50 Hz), we have $\boldsymbol{\xi}(t) = \boldsymbol{\xi}(T_s + t)$ (*periodicity constraint*). In other words, the target of the SHT method is to find an initial condition such that the power system works in periodic steady-state, viz. its time evolution satisfies the periodicity constraint. To do so, the SHT method resorts to an iterative process.[4] At each iteration, $\boldsymbol{\xi}(t + T_s)$ is computed through (1) by executing a time-domain simulation that lasts T_s only and that starts from a given initial condition for $\boldsymbol{\xi}(t)$. The next iteration is repeated using a new and possibly better $\boldsymbol{\xi}(t)$ initial condition, for example computed by the Newton method. If the current iteration is the first one, an initial guess is made. The Newton method stops when the equation $\boldsymbol{\xi}(t) = \boldsymbol{\xi}(T_s + t)$ is satisfied with an adequate accuracy, i.e., the large-signal periodic steady-state solution, referred to as $(\boldsymbol{\xi}_s(t), \boldsymbol{\zeta}_s(t))$, is found.

(ii) Assume to perturb (1) by adding the $\boldsymbol{\eta}(t) = \boldsymbol{E}_\eta e^{\dot{\imath}\omega_\eta t} + \boldsymbol{E}_\eta^* e^{-\dot{\imath}\omega_\eta t}$ small signal perturbation of period $T_\eta = 2\pi/\omega_\eta$ to the algebraic equation only for simplicity ($\dot{\imath}$ is the imaginary unit and * is the complex conjugation operator). So doing, the second set of equations in (1) becomes $\mathbf{0} = \boldsymbol{G}(\boldsymbol{\xi}(t), \boldsymbol{\zeta}(t)) + \boldsymbol{\eta}(t)$. As better specified later, $\boldsymbol{\eta}(t)$ collects the small-signal perturbations injected to derive impedances and transimpedances. At this stage, the goal is to evaluate how $\boldsymbol{\eta}(t)$ affects the small-signal solution, referred to as $(\boldsymbol{\xi}_\eta(t), \boldsymbol{\zeta}_\eta(t))$. To this aim, we assume that the small-signal solution superimposes to the $(\boldsymbol{\xi}_s(t), \boldsymbol{\zeta}_s(t))$ large-signal one; by linearizing (1) along the latter, we obtain

$$\begin{cases} \boldsymbol{\Lambda}\dfrac{d\boldsymbol{\xi}_\eta}{dt} = \left.\dfrac{\partial \boldsymbol{F}}{\partial \boldsymbol{\xi}}\right|_{\boldsymbol{\xi}_s,\boldsymbol{\zeta}_s} \boldsymbol{\xi}_\eta + \left.\dfrac{\partial \boldsymbol{F}}{\partial \boldsymbol{\zeta}}\right|_{\boldsymbol{\xi}_s,\boldsymbol{\zeta}_s} \boldsymbol{\zeta}_\eta \\ \mathbf{0} = \left.\dfrac{\partial \boldsymbol{G}}{\partial \boldsymbol{\xi}}\right|_{\boldsymbol{\xi}_s,\boldsymbol{\zeta}_s} \boldsymbol{\xi}_\eta + \left.\dfrac{\partial \boldsymbol{G}}{\partial \boldsymbol{\zeta}}\right|_{\boldsymbol{\xi}_s,\boldsymbol{\zeta}_s} \boldsymbol{\zeta}_\eta + \boldsymbol{\eta} \end{cases} . \tag{2}$$

In the equation above, some dependencies on t have been omitted for brevity. Note that the $\left.\frac{\partial \boldsymbol{F}}{\partial \boldsymbol{\xi}}\right|_{\boldsymbol{\xi}_s,\boldsymbol{\zeta}_s}$, $\left.\frac{\partial \boldsymbol{F}}{\partial \boldsymbol{\zeta}}\right|_{\boldsymbol{\xi}_s,\boldsymbol{\zeta}_s}$, $\left.\frac{\partial \boldsymbol{G}}{\partial \boldsymbol{\xi}}\right|_{\boldsymbol{\xi}_s,\boldsymbol{\zeta}_s}$, and $\left.\frac{\partial \boldsymbol{G}}{\partial \boldsymbol{\zeta}}\right|_{\boldsymbol{\xi}_s,\boldsymbol{\zeta}_s}$ terms in (2) are matrices of known periodic functions. Strictly speaking, there can be a finite set of time instants where they do not exist since $\boldsymbol{F}$ or $\boldsymbol{G}$ are discontinuous (for example we may have switching of electric elements). The use of the saltation matrices "regularize" derivatives as described in [38,39]. This makes advantageous the use of PAC with respect to methods formulated in the frequency domain. These terms implement the linearization of the (1) large-signal model of the power system along its $(\boldsymbol{\xi}_s(t), \boldsymbol{\zeta}_s(t))$ periodic steady-state solution (previously obtained with the SHT method).

Since we are looking for a periodic solution of (2), this set of linear DAEs is augmented by the periodicity constraint

$$\mathbf{0} = \boldsymbol{\xi}_s(t + kT_s) + \boldsymbol{\xi}_\eta(t + kT_s) - \boldsymbol{\xi}_s(t) - \boldsymbol{\xi}_\eta(t) = \boldsymbol{\xi}_\eta(t + kT_s) - \boldsymbol{\xi}_\eta(t) , \tag{3}$$

where kT_s is the least common multiple of the T_s and T_η periods.[5] The $\boldsymbol{\xi}_\eta(t)$ solution can be written as [41]

$$\begin{aligned} \boldsymbol{\xi}_\eta(t) &= \int_{-\infty}^{+\infty} \boldsymbol{C}(\dot{\imath}\omega; t)\left(\boldsymbol{E}_\eta \delta(\omega - \omega_\eta) + \boldsymbol{E}_\eta^* \delta(\omega_\eta - \omega)\right) e^{\dot{\imath}\omega t} d\omega \\ &= \sum_{\ell=-\infty}^{\ell=+\infty} \int_{-\infty}^{+\infty} \boldsymbol{C}_\ell(\dot{\imath}\omega)\left(\boldsymbol{E}_\eta \delta(\omega - \omega_\eta) + \boldsymbol{E}_\eta^* \delta(\omega_\eta - \omega)\right) \\ &\quad \times e^{\dot{\imath}\left(\ell\frac{\omega_s}{k} + \omega\right)t} d\omega \end{aligned} , \tag{4}$$

where $\delta(\cdot)$ is Dirac's delta function, $\omega_s = 2\pi/T_s$, and $\boldsymbol{C}_\ell \in \mathbb{C}^{N\times N}$ are complex matrices.[6] It is worth noticing that $\boldsymbol{\xi}_\eta(t)$ in (4) includes harmonics from the large steady-state solution of the system that up/down convert the ω_η angular frequency of $\boldsymbol{\eta}(t)$.

(iii) Small-signal tones $\boldsymbol{\eta}(t)$ at different discrete angular frequencies ω_η from a given frequency grid are applied to the (2) linearized periodic model (i.e., frequency scan is performed). The corresponding small-signal solutions $\boldsymbol{\xi}_\eta(t)$ for each value of ω_η are collected by solving (2) in the *time domain* as we did for (1).[7] Thus, at each value of the frequency grid, $\boldsymbol{\xi}_\eta(t)$ is computed and samples are extracted on an evenly spaced time grid of samples. A fast Fourier transform (FFT) is performed on these samples and the $\boldsymbol{C}_\ell$ coefficients are computed [42]. Note that this frequency scan can be performed in parallel on the frequency grid to boost efficiency. To this aim, we implemented a parallel multi-thread version of the PAC analysis.

2.3. The MMC admittance model

The MMC admittance model obtained with the PAC analysis is richer than a *classical* admittance model derived under the assumption that the linearized circuit model is LTI. In fact, Eq. (4) unveils the fact that when applying a small sinusoid to a LTV periodic circuit, the circuit responds with sinusoids at many frequencies. On the contrary, when applying a small sinusoid to a LTI circuit, the steady-state response is a sinusoid at the same frequency.

To better comprehend the results presented in the following section, here we shortly elaborate on the meaning of some $\boldsymbol{C}_\ell$ coefficients in (4) by considering as an example Fig. 1(e) (which is duly described later). Assume injecting a small-signal disturbance through the voltage source

[3] The modified nodal analysis (MNA) adds currents of "bad-branches" (i.e., elements with electrical characteristics that are not defined on a voltage-basis) among the unknowns. MNA facilitates managing non-linear elements with implicit characteristics that depend on port voltages and currents, and writing of differential–algebraic equations. Textbook descriptions of MNA can be found in [34,35].

[4] The interested reader can refer to Aprille and Trick [31] and Parker and Chua [32] for more details about this method.

[5] Note that k can be $\gg 1$ thus making the computation of the solution of (2) augmented with (3) very time consuming. For this reason, at this step, efficient strategies (not presented here) are exploited to overcome this issue. The interested reader can refer to Telichevesky et al. [40].

[6] In principle the (bilateral) index K should be infinite, but for practical reasons it is truncated to a custom number of harmonics. In this paper, $K = 20$ for all simulations.

[7] We mainly mention the $\boldsymbol{\xi}_\eta(t)$ state variables because, assuming we are dealing with semi-explicit index-1 differential algebraic equations, the $\boldsymbol{\zeta}_\eta(t)$ algebraic variables can be directly derived from the former as $\boldsymbol{\zeta}_\eta = -\left(\left.\frac{\partial \boldsymbol{G}}{\partial \boldsymbol{\zeta}}\right|_{\boldsymbol{\xi}_s,\boldsymbol{\zeta}_s}\right)^{-1}\left(\left.\frac{\partial \boldsymbol{G}}{\partial \boldsymbol{\xi}}\right|_{\boldsymbol{\xi}_s,\boldsymbol{\zeta}_s} \boldsymbol{\xi}_\eta + \boldsymbol{\eta}\right)$.

$\eta_a(t)$ (i.e., an entry of $\boldsymbol{\eta}(t)$) and wanting to examine the resulting small-signal current $i_p(t)$ at the DC side of the MMC (i.e., an entry of $\boldsymbol{\xi}_\eta(t)$ or $\boldsymbol{\zeta}_\eta(t)$).

A suitable entry of the $\boldsymbol{C}_0$ matrix (i.e., the FFT DC component) relates the frequency component of $i_p(t)$ at the same frequency of the inject signal $\eta_a(t)$. Thus, this entry of $\boldsymbol{C}_0$ corresponds to an admittance, that is, the ratio between a current and voltage phasor [43], viz. two complex numbers corresponding to two sinusoids at the same frequency.

Strictly speaking, this does not hold for the other corresponding entries of the $\boldsymbol{C}_\ell$ ($\ell \neq 0$) coefficients, as they relate $\eta_a(t)$ to components of $i_p(t)$ at a different frequency range. Indeed, the ℓ index identifies the $\ell\times 2\pi\times 50\,\text{Hz}$ harmonic of up/down-conversion. For instance, $\boldsymbol{C}_{-1}$ and $\boldsymbol{C}_{+1}$ include respectively the $i_p(t)$ spectra components at $(\omega_\eta - 2\pi\times 50\,\text{Hz})$ and $(\omega_\eta + 2\pi\times 50\,\text{Hz})$. Nonetheless, for simplicity, we still use the term admittance or trans-admittance also in these cases.

In the following, we will show that the information brought by the $\boldsymbol{C}_\ell$ ($\ell \neq 0$) coefficients may be relevant in predicting instability issues in cases in which the only $\boldsymbol{C}_0$ matrix i.e., the canonical impedance model, fails.

3. PAC analysis of the DCS1 test system

3.1. Simulation setting

To show how PAC analysis operates and how it can be exploited to compute admittances and thus analyze the small-signal stability of a complex AC/DC power system, we chose to apply it to the Cigre DCS1 test system, whose schematic is shown in Fig. 1(d). All of its specifics can be found in [27]. We recap below only some key features.[8]

The HVDC link, whose pole-to-pole voltage is 400 kV, comprises two 200 km lines described by a detailed frequency-dependent model [44] (simpler models were not chosen as they can lead to erroneous results [45]). The nominal line-to-line RMS voltage of AC1 and AC2 systems is 145 and 380 kV, respectively. MMC1 and MMC2, whose rated power is 800 MW, operate in the P,Q and DC-SLACK,Q mode, respectively.[9] Unless otherwise stated, MMC1 injects 400 MW in the HVDC link and the reactive power exchange is zero for both MMCs.

The computation of MMC (trans-)admittances requires defining during the PAC analysis a proper set of small-signal perturbations (inputs) and observed variables (outputs). Considering the representation of the MMC as a five-terminal component in Fig. 1(e), we chose as inputs the small-signal voltage sources η_a, η_b, η_c, and η_p, while as outputs the currents flowing through them (i.e., ι_a, ι_b, ι_c, and ι_p). This injection scheme, which applies to both MMC1 and MMC2, allows deriving a set of generic (trans-)admittances $Y^{\ell}_{1_m,2_q}$ [25].[10]

3.2. Validation of the PAC-based results

The first results we show are the real (Re) and imaginary (Im) part of the admittance $Y^0_{1_a,1_a}$ and trans-admittance $Y^0_{1_a,2_a}$ depicted in Figs. 2 and 3. To validate the results computed with PAC analysis, some admittance values were determined through a battery of SHT-based analyses that operated differently from what was described in step **(i)**. In this case, indeed, the large-signal steady-state solution of (1) was derived assuming that the second equation already included the small-signal perturbations $\boldsymbol{\eta}(t)$ (instead of considering them only from step **(ii)**). This means that we did not use SHT to compute the unperturbed solution of the system as in step **(i)**, but we used it to compute the perturbed solution due to the $\boldsymbol{\eta}(t)$ small signal. Then, admittances were computed by considering the ratio of the corresponding currents and voltages at (perturbed) steady-state. It is worth recalling that, contrary to step **(ii)** of PAC analysis, the SHT method does not perform any linearization of the DCS1 grid. Thus, its results are considered "exact".

Since the SHT method computes periodic large-signal solutions, the comparisons between PAC and SHT were carried out on a set of discrete frequencies that lead to a reasonable least common multiple between the $T_s = 1/50\,\text{Hz}$ working period of the MMCs and the T_η period of the injected small-signal perturbations. The small least common multiple limits the effort in performing the time domain analyses needed by the SHT method. The very good agreement between the results obtained with the SHT method and PAC analysis (i.e., • markers and solid lines) validates the latter.[11]

3.3. Mutual interactions between MMC1 and MMC2

For what concerns $Y^0_{1_a,2_a}$ in Fig. 3, it is also worth pointing out that the magnitude of $Y^0_{1_a,2_a}$ is not zero, but rather approximately 1/10 that of $Y^0_{1_a,1_a}$. This means that disturbances in the AC1 system (e.g., voltage fluctuations due to stochastic nature of wind and solar parks connected to the network) propagate through the HVDC link to the AC2 system attenuated by ten times [46]. An harmonic down-conversion from system AC2 to the HVDC link and a subsequent up-conversion from the latter to grid AC1 can constitute one among several frequency "paths" to propagate disturbances between the two networks. This path is further detailed in Section 3.6.

3.4. MMC1 AC-side instability

We now analyze possible instabilities at the AC-side of MMC1. We first consider the $Y^0_{1_a,1_a}$ admittance to check if it shows frequency intervals where its $\text{Re}\{Y^0_{1_a,1_a}\}$ real part is negative: this feature is of interest, since negative impedances/admittances can severely threaten power system stability [47]. Then, we consider $Y^2_{1_a,1_a}$, i.e., frequency up-conversion and in particular how perturbations are up-converted by MMC1 in the right portion of the spectrum above 100 Hz (second harmonic). Also in this case, we look for frequency intervals where $\text{Re}\{Y^2_{1_a,1_a}\} < 0$ as possible cause of instability. We underline that the outcome of this analysis depends not only on the design of the DCS1 system per se, but also on the AC grids connected to it.

Fig. 4 shows the real and imaginary part of the admittance $Y^0_{1_a,1_a}$ in two cases: MMC1 injects (red traces) and absorbs (black traces) 400 MW in/from the HVDC link. As expected, $\text{Re}\{Y^0_{1_a,1_a}\}$ is positive or negative in

[8] The simulation results shown hereafter were obtained through the academic simulator PAN [20–22]. The files needed to run the simulations are available on GitHub at https://github.com/Davide-del-Giudice/mmc_impedance.git.

[9] With reference to the *outer power loop* in Fig. 1(c), it means that MMC1 regulates active and reactive power exchange, whereas MMC2 controls the DC-side voltage and reactive power exchange.

[10] In particular, 1_m and 2_q denote respectively the injection and collection points (with 1 and 2 identifying the AC1 or AC2 grid, respectively), while ℓ is the harmonic index. This is a compact way to write $Y_{1_m,2_q}(\omega_\eta + \ell\omega_s)$. For instance, $Y^0_{1_a,1_a}$ is obtained by injecting a small-signal voltage in the phase-a by η_a in the AC1 AC system in Fig. 1(d) and collecting the corresponding i_a current at the same frequency (i.e., the 0 harmonic is considered).

[11] Based on the above, one could question the necessity of steps **(ii–iii)** of the PAC analysis. Besides, since it computes an "exact" solution, one might as well only execute the SHT method with the $\boldsymbol{\eta}(t)$ perturbation turned on, as described before. To clear this suspicion, consider the • marker in Fig. 2 at 5 Hz (vertical dashed line). The least common multiple between $T_s = 20\,\text{ms}$ and $T_\eta = 1/5 = 200\,\text{ms}$ is $200\,\text{ms} = 10\times T_s$, which means that the SHT method takes 10× the CPU time needed to compute the solution at step **(i)**. This CPU time is comparable to that overall required by the PAC analysis to perform the frequency scan on the *entire* frequency grid consisting of 741 samples. If we repeated the SHT method at each sample of the frequency grid, the computational burden would be prohibitive. On the contrary, with its three steps, the PAC analysis reduces CPU time at the cost of a minor accuracy loss.

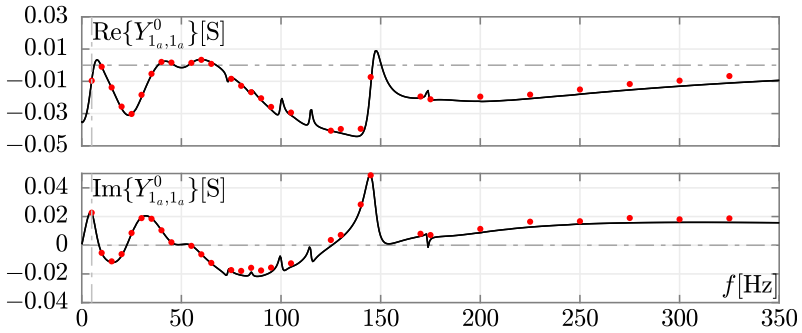

Fig. 2. The real and imaginary part of $Y^0_{1_a,1_a}$. Solid lines and • marks respectively denote the results obtained with PAC analysis and SHT method (the latter at discrete frequency values). x-axis: frequency [Hz], y-axis: admittance [S = Ω^{-1}]. In each panel, the horizontal dashed lines denote zero real or imaginary part.

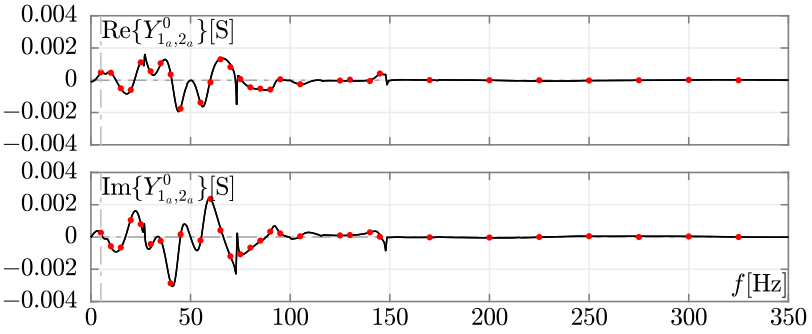

Fig. 3. The real and imaginary part of $Y^0_{1_a,2_a}$. Solid lines and • marks respectively denote the results obtained with PAC analysis and SHT method (the latter at discrete frequency values). x-axis: frequency [Hz], y-axis: admittance [S]. In each panel, the horizontal dashed lines denote zero real or imaginary part.

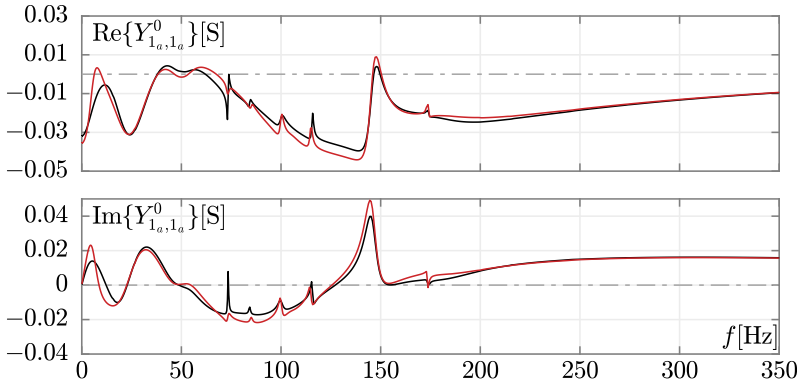

Fig. 4. The real and imaginary part of $Y^0_{1_a,1_a}$ obtained by considering MMC1 in two cases: 400 MW power injection (red traces) and absorption (black traces) into/from the DC grid. The red traces are a replica of those in Fig. 3. x-axis: frequency [Hz], y-axis: admittance [S]. In each panel, the horizontal dashed lines denote zero real or imaginary part.

a narrow interval around 50 Hz depending on the direction of the active power exchange. This can be a peculiarity of the converters working in PQ mode. A hint on this characteristic can be derived by considering a single-phase constant power load that exchanges only active power $P_{\text{ph}}(t)$. We have $v_{\text{ph}}(t)i_{\text{ph}}(t) = P_{\text{ph}}(t)$, with $v_{\text{ph}}(t)$ and $i_{\text{ph}}(t)$ being the phase voltage and current of the constant power load. The differential admittance is $Y_{\text{ph}}(t) = {}^{\partial i_{\text{ph}}(t)}/_{\partial v_{\text{ph}}(t)} = -{}^{P_{\text{ph}}(t)}/_{v^2_{\text{ph}}(t)}$. We see that the sign of $Y_{\text{ph}}(t)$ depends on that of $P_{\text{ph}}(t)$ (i.e., whether $P_{\text{ph}}(t)$ is absorbed or injected). We anticipate that the corresponding admittance on the DC side has a similar but complementary characteristic because an MMC working in P,Q mode exchanges almost the same power on both the AC and DC sides: what changes is the sign of the exchanged power.

In both cases reported in Fig. 4, $\text{Re}\{Y^0_{1_a,1_a}\} < 0$ in most of the frequency range considered. Other than showing a complex frequency dependence, $\text{Im}\{Y^0_{1_a,1_a}\}$ is also positive in some frequency intervals, which means that the MMC exhibits a capacitive behavior. This might trigger instabilities when MMC1 is connected to a weak AC grid, characterized by large inductive impedances that may couple with this capacitive behavior and lead to an unstable resonator because $\text{Re}\{Y^0_{1_a,1_a}\}$ is negative. This might occur even if both the active and reactive MMC1 power set-points are zero.

To validate this statement, we considered again the HVDC system in Fig. 1(d). In this case, both the active and reactive power set-points of MMC1 were zero,[12] and a strong and a weak three-phase line were connected in parallel between grid AC1 and transformer TR1 in Fig. 1.[13]

[12] Since we modified the set-point of MMC1, its $Y^0_{1_a,1_a}$ admittance changes. We do not show it in this new set-point since its main characteristics in the frequency interval of interest do not change significantly.

[13] The resistances and inductances of the strong line are $r = 23.2\,\text{m}\Omega$, $l = 0.739\,\text{mH}$; they are derived from the specifications at page 152 of B4-57 [27], i.e., the short circuit power is 30 GVA and the R/X ratio is 0.1.

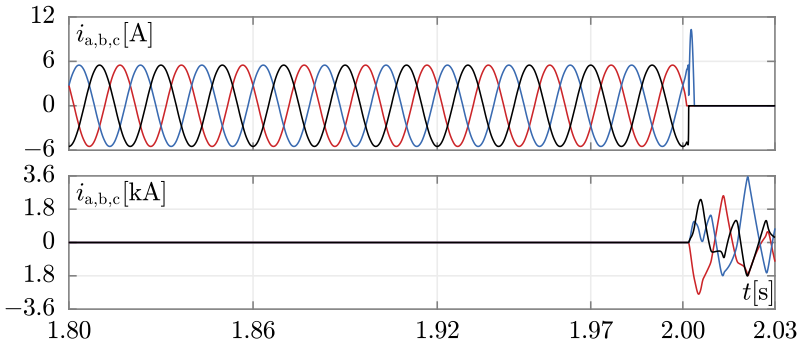

Fig. 5. The three-phase currents in the strong line (upper panel) and in the weak line (lower panel). x-axis: frequency [Hz], y-axis: current [A].

This configuration can be considered as a simplification of a more complex one where MMC1 is connected to grid AC1 through two lines. The strong line offers a direct (short) connection of the MMC to the grid. On the contrary, assuming that MMC1 operates in a meshed grid, the weak line represents an additional, longer path between the converter and grid AC1.

We simulated this hybrid system and tripped the breakers of the strong line at 2 s. Following the previous example, this event could mirror the fact that the strong line is disconnected (e.g., for maintenance), but MMC1 is still connected to grid AC1 through the weak line. Since the active and reactive power setpoint of the converter are zero, the power exchange is well below the power transmission capabilities of the weak line. However, as shown in the following, the system becomes unstable.

The three-phase currents in the two lines after and before line tripping are reported in Fig. 5. Before line tripping, the current magnitude in both lines is very low due to the zero power set-points, as expected. The small currents flowing are only due to the conduction and switches losses of the MMC1 and other system components. At 2 s, the currents in the strong line become zero due to line tripping. On the contrary, those of the weak line diverge significantly with peaks at several kA,[14] which confirms that system instability is induced by the weak AC grid connected to MMC1 working in P,Q mode [48]. To the best of the authors' knowledge, this weak design aspect was not reported in [27], which describes the DCS1 test system.

The $Y^2_{1_a,1_a}$ transfer function reported in Fig. 6 shows the relation between the small-signal η_a injected voltage perturbation at the ω_η angular frequency and the up-converted effects at the $\omega_\eta + 2\omega_s$ second harmonic of the current flowing through the voltage source injecting the perturbation. We improperly refer to this transfer function as "admittance". In Fig. 6 we report also $Y^0_{1_a,1_a}$ for comparisons. The $Y^0_{1_a,1_a}$ and $Y^2_{1_a,1_a}$ admittances were derived with MMC1 injecting 800 MW in the DC grid. The impedance of the AC grid to which MMC1 is connected was increased, i.e., the connection was weakened.

By observing $\mathrm{Re}\{Y^0_{1_a,1_a}\}$ in Fig. 6, we see that it is positive at frequency close to 50 Hz with a peak value of 5 mS. From frequencies slightly above 50 Hz up to 410 Hz it is negative and above 410 Hz it becomes positive. By considering the sign of $\mathrm{Re}\{Y^0_{1_a,1_a}\}$, we do not expect MMC1 to show an unstable behavior at frequencies above 410 Hz.

The last two panels from top of Fig. 6 show the components of the $Y^2_{1_a,1_a}$ admittance. We see that $\mathrm{Re}\{Y^2_{1_a,1_a}\} > 0$ till 420 Hz, above which it becomes negative up to 590 Hz. The peak negative value of $\mathrm{Re}\{Y^2_{1_a,1_a}\}$ is at 439 Hz and at this frequency $\mathrm{Im}\{Y^2_{1_a,1_a}\} < 0$, meaning that MMC1 has an inductive behavior for small signal up-converted perturbations.[15]

If we limit our attention to the $Y^0_{1_a,1_a}$ (conventional) admittance, there is no reason to expect any system instability if we decided to add to the AC bus to which MMC1 is connected a three phase capacitive shunt that leads to a resonance frequency greater than 410 Hz ($\mathrm{Re}\{Y^0_{1_a,1_a}\}$ is positive). However if we consider $Y^2_{1_a,1_a}$, we see that the addition of the capacitive shunt of proper value can trigger instability, since we have a build-up of an undamped LC resonator in the $420 - 590$ Hz frequency range ($\mathrm{Re}\{Y^2_{1_a,1_a}\} < 0$).

To check this instability onset, we performed a transient stability analysis. Fig. 7 shows the obtained current through the phase-a of the MMC1 (i.e., the same phase where the small signal has been injected). Oscillations superimposed to the 50 Hz phase-a current are clearly visible. The frequency of these oscillations cannot be easily determined since the non-linear model of the DCS1 test system leads to a rich dynamic composed of several harmonics. However, on average different frequency measures performed in consecutive time intervals lead to 437 Hz, which is consistent with the $Y^2_{1_a,1_a}$ admittance traces reported in Fig. 6.

We underline that this result can be captured only if frequency up-conversion (down-conversion) is considered, i.e, if LTV small-signal models are used instead of LTI ones. Contrary to the canonical small-signal analysis approaches mentioned in the introduction, the PAC analysis easily gives this kind of information to HVDC system designers.

3.5. MMC1 DC-*side instability*

We now focus on the DC side of MMC1. Fig. 8 shows the real and imaginary part of $Y^0_{1_p,1_p}$ in two cases. In the first one, MMC1 injects 800 MW into the DC grid, while in the second one the same power is absorbed instead. MMC1 works at unity power factor in both cases. By referring to Fig. 1(e), $Y^0_{1_p,1_p}$ was computed with the PAC analysis by acting on η_p at AC1 and collecting the corresponding i_p current at the same frequency.

The real part of the admittance is positive (negative) in the first (second) case at frequencies close to 0 Hz (DC). As already stated, this

The resistance and inductance of the weak line are $r = 16\,\Omega$, $l = 200$ mH, corresponding to a short circuit power of 108 MVA and an R/X ratio of 0.255. The parameters of the synchronous generator modeled in the DQ0-frame are: prating = 610 MW, vrating = 83.7 kV, xl = 0.2396, ra = 0, xd = 0.8979, xdp = 0.2998, xds = 0.23, td0p = 7.4, td0s = 0.03, xq = 0.646, xqp = 0.646, xqs = 0.4, tq0p = 0, tq0s = 0.033, m = 10.296, d = 2.

[14] Currents do not diverge due to several reasons such as for example the intervention of the over-current protections.

[15] Notice that $Y^0_{1_a,1_a}$ and $Y^1_{1_a,1_a}$ span over different frequency ranges. This is due to the fact that $Y^2_{1_a,1_a}$ mirrors frequency up conversion (second harmonic). In this case, the f-axis must be read as $2f_s + \frac{1}{T_\eta}$, with f_s being the steady-state frequency of the unperturbed system (i.e., 50 Hz). For example, a small-signal perturbation at $\frac{1}{T_\eta} = 1$ Hz up folds at 100 Hz+1 Hz in the frequency axis. Similar considerations will be made, where needed, in the other examples that follow.

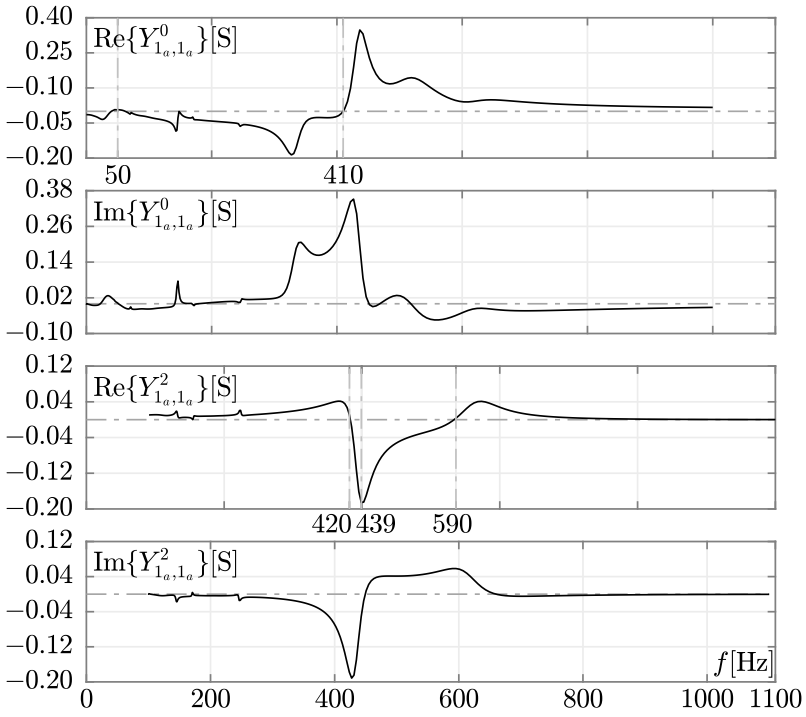

Fig. 6. The first trace from top shows Re{$Y^0_{1_a,1_a}$}; the second trace from top shows Im{$Y^0_{1_a,1_a}$}; the third trace shows Re{$Y^2_{1_a,1_a}$} and finally the bottom trace shows Im{$Y^2_{1_a,1_a}$}. x-axis: frequency [Hz], y-axis: admittance [S]. In each panel, the horizontal dashed lines denote zero real or imaginary part.

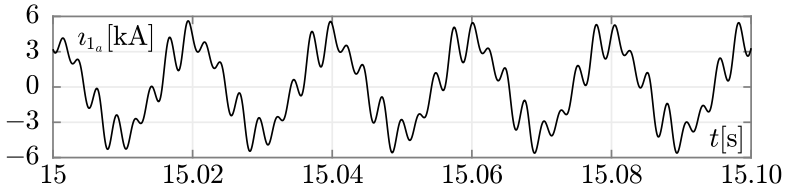

Fig. 7. The phase-a current of the MMC1 obtained with the transient stability analysis when a three-phase shunt capacitor is connected at the same AC bus of the converter. x-axis: time [s], y-asix: current [A].

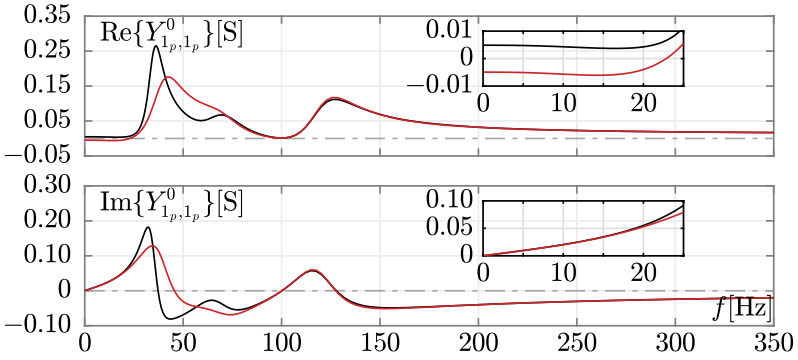

Fig. 8. The real and imaginary part of $Y^0_{1_p,1_p}$ obtained by considering MMC1 in Fig. 1(d) in two cases: 800 MW power injection (black traces) and absorption (red traces) into/from the DC grid. x-axis: frequency [Hz], y-axis: admittance [S]. In each panel, the horizontal dashed lines denote zero real or imaginary part.

is an expected result due to the peculiarity of the P,Q configuration of MMC1 working with the two power settings.[16] In addition, the imaginary part of $Y^0_{1_p,1_p}$ in the two cases has a complex frequency behavior, taking both positive and negative values in different frequency intervals.

To show the implications of these shapes on stability, consider the insets of Fig. 8, which better show Re{$Y^0_{1_p,1_p}$} and Im{$Y^0_{1_p,1_p}$} for

[16] The MMC controllers are equipped with input low-pass filters, some of which have a cut-off frequency of 11 Hz. Thus, controllers do not properly regulate above this frequency. Concerning the admittance sign, being P_{dc} the positive *constant* power absorbed from the DC side (i.e., second case), we have $P_{dc} = v_{dc} i_{dc}$ and thus $i_{dc} = P_{dc}/v_{dc}$. So, the differential admittance is $di_{dc}/dv_{dc} = -P_{dc}/v^2_{dc} < 0$. Note that P_{dc} has an opposite sign with respect to P_{ph} described in Section 3.4.

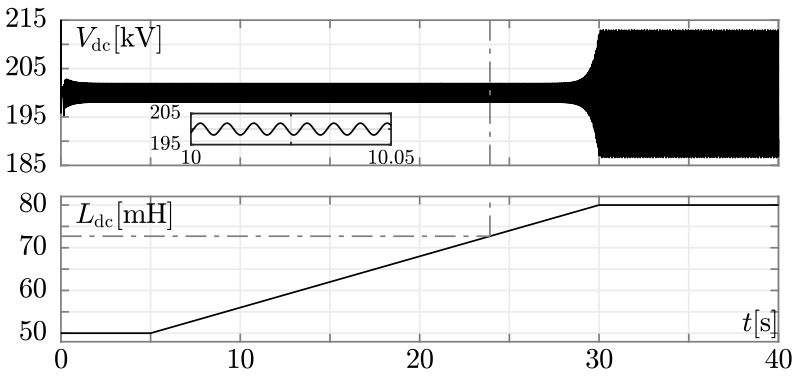

Fig. 9. Upper panel: voltage at the positive DC pole (in [kV]) ; Lower panel: value of the series inductor (in [mH]). x-axis: frequency [Hz].

frequencies lower than 25 Hz (i.e., the region where in the second case $\mathrm{Re}\{Y^0_{1_p,1_p}\} < 0$). In this range $\mathrm{Im}\{Y^0_{1_p,1_p}\}$ is positive in both cases, meaning that the MMC has a capacitive-type susceptance. Instability occurs if the DC side of MMC1 is connected to an HVDC link with an inductive-type reactance large enough to form a resonant circuit with a frequency falling in the interval where $\mathrm{Re}\{Y^0_{1_p,1_p}\} < 0$. For example, this may happen when inductor-based fault current limiters are inserted at the MMC DC port [49,50].

Let us consider for instance the imaginary part of $Y^0_{1_p,1_p}$ in the second case at $f_r = 20$ Hz, which is 54.7 mS. This frequency is chosen so that $\mathrm{Im}\{Y^0_{1_p,1_p}\}$ is as large as possible and so is frequency, while $\mathrm{Re}\{Y^0_{1_p,1_p}\}$ is still negative with some margin. The susceptance of $Y^0_{1_p,1_p}$ is modeled by $c = {}^{54.7\,\mathrm{mS}}/_{(2\pi f_r)} = 435$ μF. Assume now to insert an inductor at each pole of MMC1 (i.e., bus **dc1** in Fig. 1(d)). DC-side instability occurs if $l \geq {}^{0.5}/_{[c(2\pi f_r)^2]} = 72.7$ mH per pole.[17]

To support this claim, we performed a transient stability analysis of the modified version of the DCS1 test system by considering the second case (i.e., 800 MW power absorbed from the DC grid) and slowly increasing the value of each pole inductance from 50 mH up to 80mH. Fig. 9 reports the obtained results. The onset of instability around the selected inductance value is confirmed by the divergence in DC-side voltage, which is eventually stopped by the presence of "limiters" in the MMC control scheme. On the contrary, instability does not occur in the first case since $\mathrm{Re}\{Y^0_{1_p,1_p}\} > 0$ in the entire frequency range we considered.

3.6. Analysis of frequency up/down conversion phenomena

We now present the last simulation set of this section, which is specifically devoted to analyzing through PAC one of the possible frequency conversion chains that provides a path for disturbance propagation from the AC2 to the AC1 system.

We first considered as perturbation the small-signal voltage η_a on the phase-a of the AC2 system and collected the corresponding voltage across the p and n nodes of the DC side of MMC1 (i.e., v_{pn}). Specifically, we analyzed the frequency down-conversion of this voltage through MMC2. The resulting transfer function that we derived is $H^{-1}_{2_a,1_{pn}} = H_{2_a,1_{pn}}(\omega_\eta + \ell\omega_s)$, with $\ell = -1$. This means that, when ω_η is close to ω_s, MMC2 down-converts the small-signal of its AC-side voltage in a frequency range close to the DC component. In turn, this converted small-signal propagates through the HVDC link to MMC1.

[17] At f_r, $\mathrm{Re}\{Y^0_{1_p,1_p}\} < 0$. Thus, the addition of l to c forms an unstable resonator. If l were increased, the resonance frequency should decrease, keeping $\mathrm{Re}\{Y^0_{1_p,1_p}\}$ in the frequency region where it is negative and $\mathrm{Im}\{Y^0_{1_p,1_p}\}$ is positive (see Fig. 8).

Fig. 10 shows the real and imaginary part of $H^{-1}_{2_a,1_{pn}}$ computed with the PAC analysis. The x-axis refers to the frequency of the small-signal voltage v_{pn} mentioned earlier. The angular frequency of this voltage amounts to $\omega_{\mathrm{pn}} = |\omega_\eta - \omega_s|$ (i.e., the frequency axis in Fig. 10 has to be considered from *right to left*). For example, being $\omega_s = 2\pi \times 50$ Hz, a small-signal perturbation at $\omega_\eta = 2\pi \times 1$ Hz folds at |1 Hz − 50 Hz| in the frequency axis. From Fig. 10 one can notice that the magnitude of the traces at frequencies lower than 10 Hz is not zero. This means that perturbations above 40 Hz in the AC2 system are down-converted in the HVDC link with non-negligible magnitudes at frequencies below 10 Hz.

As next step, we considered the frequency up-conversion of the small-signal perturbation in the HVDC link by MMC1. In particular, this frequency up-conversion is modeled by the $Y^{+1}_{1_p,1_a} = Y_{1_p,1_a}(\omega_\eta + \ell\omega_s)$, transfer function with $\ell = +1$. $Y^{+1}_{1_p,1_a}$ is such that the previously mentioned perturbations close to the DC component appear close to 50 Hz in the AC1 system. The composition of $H^{-1}_{2_a,1_{pn}}$ and $Y^{+1}_{1_p,1_a}$ gives the coupling path through the $\ell = -1$ and $\ell = +1$ frequency conversion from AC2 to AC1 grids.

The $Y^{+1}_{1_p,1_a}$ transfer function is shown in Fig. 11 (note that the frequency axis starts from 50 Hz). A resonance peak is located close to 150 Hz. The small-signal perturbation at 50 Hz on the DC side of the MMC1 interferes with the circulating current (100 Hz) suppression controller and is up-converted close to 150 Hz in the AC1 system. If we turn off this controller, the peak disappears.

As a last comment, we point out that there are several other frequency conversion paths that couple the AC1 and AC2 systems in both directions. For instance, a negative sequence component at $-\omega_s$ can be up-converted ($\ell = +1$) close to the DC value by one MMC [51] and then down-converted still in negative sequence by the other MMC ($\ell = -1$). Albeit partial, the analysis reported here underlines that frequency up/down-conversion phenomena between MMCs are extremely complex.

4. Conclusions

In this work, we applied the periodic small-signal (PAC) analysis to the MMC-based Cigre DCS1 HVDC system. After presenting the mathematical bases of the PAC analysis, we used it to investigate possible stability issues of the DCS1 benchmark. We also analyzed some frequency up/down-conversion phenomena between the MMCs.

By exploiting the admittances computed with PAC, we investigated different stability issues. All of those stem from the fact that the real part of the (trans)admittances of MMC1 is negative in some frequency intervals. Depending on their imaginary part, the addition of either capacitive or inductive elements at some points of the system could affect system stability by leading to an unstable resonator. In particular, AC-side instabilities could be induced by connecting the HVDC system to a weak AC grid even if no active and reactive power is actually exchanged.

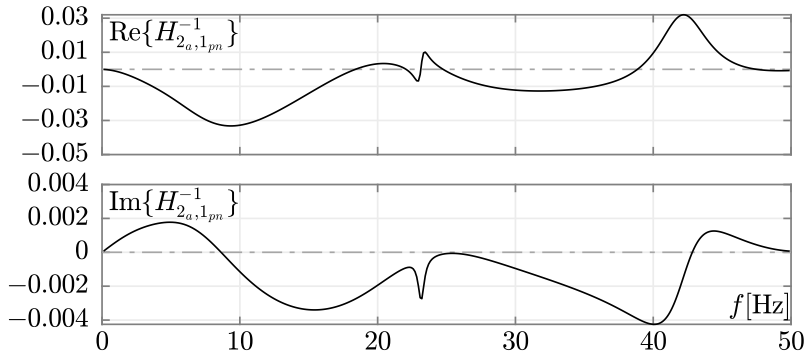

Fig. 10. The real and imaginary part of the $H^{-1}_{2_a,1_{pn}}$ transfer function, which is dimensionless. x-axis: frequency [Hz]. In each panel, the horizontal dashed lines denote zero real or imaginary part.

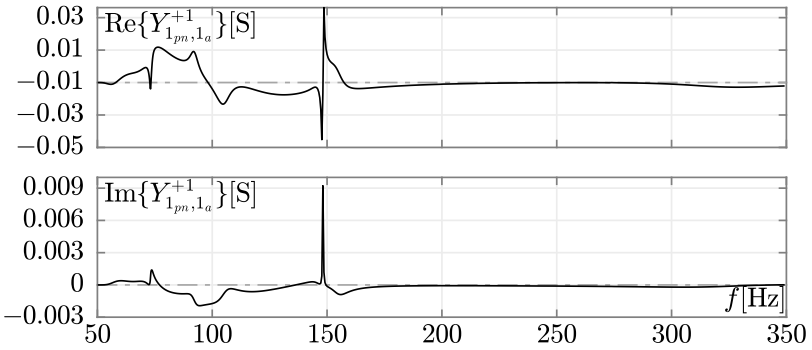

Fig. 11. The real and imaginary part of the $Y^{+1}_{1_{pn},1_a}$ transfer function. x-axis: frequency [Hz], y-axis: admittance [S]. In each panel, the horizontal dashed lines denote zero real or imaginary part.

DC-side instability could be triggered by the insertion at the DC poles of the MMC of fault current limiters made up of inductors.

Another stability issue that we analyzed is related to frequency up-conversion phenomena. In particular, AC-side instability could be induced by adding a three-phase capacitor shunt to the AC-side bus of MMC1. This stability issue can only be detected by resorting to methods capable of representing frequency folding, such as the PAC analysis.

All these examples show that the stability of the DCS1 HVDC test system (and any other benchmark grid for that matter) does not depend only on how it was originally designed as a "stand-alone" system, but also on how it is employed in more complex power systems. As a result, impedances/admittances must be computed and considered in detail on a design basis and for each peculiar working mode of the hybrid power system under study. In this context, PAC can be extremely helpful, as it allows to efficiently compute not only the impedances/admittances that can be obtained with canonical methods (i.e., those that simplify the MMC topology and control scheme so that the linearized circuit model is still LTI) but also those associated with frequency up/down conversion phenomena, which could also have an impact on power system stability.

The key feature of the PAC analysis is that it is fully numerical. Thus, other than having general validity, this approach does not require any simplification of the power system under study. For instance, when applying it to the DCS1 benchmark, the power system was analyzed *as is* (i.e., nothing, from MMC topology, controls, to protections was changed in any way while performing the PAC analyses).

CRediT authorship contribution statement

D. del Giudice: Conception and design of study, Analysis and/or interpretation of data, Writing – original draft, Writing – review & editing. **F. Bizzarri:** Conception and design of study, Analysis and/or interpretation of data, Writing – original draft, Writing – review & editing. **D. Linaro:** Conception and design of study, Analysis and/or interpretation of data, Writing – original draft, Writing – review & editing. **A. Brambilla:** Conception and design of study, Analysis and/or interpretation of data, Writing – original draft, Writing – review & editing.

Declaration of competing interest

All authors have participated in

(1) conception and design, or analysis and interpretation of the data;

(2) drafting the article or revising it critically for important intellectual content;

(3) approval of the final version.

This manuscript has not been submitted to, nor is under review at, another journal or other publishing venue.

The authors have no affiliation with any organization with a direct or indirect financial interest in the subject matter discussed in the manuscript.

Data availability

Data will be made available on request.

Acknowledgment

All authors approved the version of the manuscript to be published.

References

[1] Mathe L. Performance comparison of the modulators with balancing capability used in MMC applications. In: 2017 IEEE 26th International Symposium on Industrial Electronics (ISIE). 2017, p. 815–20. http://dx.doi.org/10.1109/ISIE.2017.8001351.

[2] Franquelo LG, Rodriguez J, Leon JI, Kouro S, Portillo R, Prats MAM. The age of multilevel converters arrives. IEEE Ind Electron Mag 2008;2(2):28–39.

[3] Lesnicar A, Marquardt R. An innovative modular multilevel converter topology suitable for a wide power range. In: Power Tech Conference Proceedings, Bologna, vol. 3. IEEE; 2003, p. 6–10.

[4] Dekka A, Wu B, Fuentes RL, Perez M, Zargari NR. Evolution of topologies, modeling, control schemes, and applications of modular multilevel converters. IEEE J Emerg Sel Top Power Electron 2017;5(4):1631–56.

[5] del Giudice D, Bizzarri F, Linaro D, Brambilla A. Modular multilevel converters: Key features, control strategies and main challenges. Springerbriefs in applied sciences and technology, 2023, p. 11–50.

[6] Wang Y, Zhao C, Guo C. Comparison study of small-signal stability of MMC-HVDC system in different control modes. Int J Electr Power Energy Syst 2019;111:425–35. http://dx.doi.org/10.1016/j.ijepes.2019.04.017, URL: https://www.sciencedirect.com/science/article/pii/S0142061518326358.

[7] Zhang Y, Zhang J, Deng F, Din Z. Voltage balancing control of hybrid MMC under over-modulation situations with optimal circulating current injection. Int J Electr Power Energy Syst 2022;140:108053. http://dx.doi.org/10.1016/j.ijepes.2022.108053, URL: https://www.sciencedirect.com/science/article/pii/S0142061522000953.

[8] Wu H, Wang X. Dynamic impact of zero-sequence circulating current on modular multilevel converters: Complex-valued AC impedance modeling and analysis. IEEE J Emerg Sel Top Power Electron 2020;8(2):1947–63. http://dx.doi.org/10.1109/JESTPE.2019.2951446.

[9] Zhu S, Qin L, Liu K, Ji K, Li Y, Huai Q, Liao X, Yang S. Impedance modeling of modular multilevel converter in D-Q and modified sequence domains. IEEE J Emerg Sel Top Power Electron 2020;1. http://dx.doi.org/10.1109/JESTPE.2020.3028079.

[10] Zhu S, Liu P, Liao X, Qin L, Huai Q, Xu Y, Li Y, Wang F. D-Q frame impedance modeling of modular multilevel converter and its application in high-frequency resonance analysis. IEEE Trans Power Deliv 2020;1. http://dx.doi.org/10.1109/TPWRD.2020.3010873.

[11] Lyu J, Zhang X, Cai X, Molinas M. Harmonic state-space based small-signal impedance modeling of a modular multilevel converter with consideration of internal harmonic dynamics. IEEE Trans Power Electron 2019;34(3):2134–48. http://dx.doi.org/10.1109/TPEL.2018.2842682.

[12] Liu Y, Zheng J, Chen Q, Duan Z, Tian Y, Ban M, Li Z. MMC-STATCOM supplementary wide-band damping control to mitigate subsynchronous control interaction in wind farms. Int J Electr Power Energy Syst 2022;141:108171. http://dx.doi.org/10.1016/j.ijepes.2022.108171, URL: https://www.sciencedirect.com/science/article/pii/S0142061522002058.

[13] Xu Z, Li B, Han L, Hu J, Wang S, Zhang S, Xu D. A complete HSS-based impedance model of MMC considering grid impedance coupling. IEEE Trans Power Electron 2020;35(12):12929–48. http://dx.doi.org/10.1109/TPEL.2020.2996714.

[14] Love GN, Wood AR. Harmonic State Space model of power electronics. In: 2008 13th International Conference on Harmonics and Quality of Power. 2008, p. 1–6. http://dx.doi.org/10.1109/ICHQP.2008.4668792.

[15] Sakinci OC, Beerten J. Generalized dynamic phasor modeling of the MMC for small-signal stability analysis. IEEE Trans Power Deliv 2019;34(3):991–1000. http://dx.doi.org/10.1109/TPWRD.2019.2898468.

[16] Mattavelli P, Stankovic A, Verghese G. SSR analysis with dynamic phasor model of thyristor-controlled series capacitor. IEEE Trans Power Syst 1999;14(1):200–8. http://dx.doi.org/10.1109/59.744524.

[17] Okumura M, Sugawara T, Tanimoto H. An efficient small signal frequency analysis method of nonlinear circuits with two frequency excitations. IEEE Trans Comput-Aided Des Integr Circuits Syst 1990;9(3):225–35. http://dx.doi.org/10.1109/43.46798.

[18] Brambilla A, Gruosso G, Redaelli MA, Storti Gajani G, Caviglia D. Improved small signal analysis for circuits working in periodic steady state. IEEE Trans Circuits Syst I 2010;57(2):427–37.

[19] Mehrmann V, Wunderlich L. Hybrid systems of differential-algebraic equations - Analysis and numerical solution. J Process Control 2009;19(8):1218–28.

[20] Linaro D, del Giudice D, Bizzarri F, Brambilla A. PanSuite: A free simulation environment for the analysis of hybrid electrical power systems. Electr Power Syst Res 2022;212.

[21] Bizzarri F, Brambilla A. PAN and MPansuite: Simulation vehicles towards the analysis and design of heterogeneous mixed electrical systems. In: NGCAS. IEEE; 2017, p. 1–4.

[22] Bizzarri F, Brambilla A, Gajani GS, Banerjee S. Simulation of real world circuits: Extending conventional analysis methods to circuits described by heterogeneous languages. IEEE Circuits Syst Mag 2014;14(4):51–70. http://dx.doi.org/10.1109/MCAS.2014.2360803.

[23] Bizzarri F, del Giudice D, Linaro D, Brambilla A. Numerical approach to compute the power flow solution of hybrid generation, transmission and distribution systems. IEEE Trans Circuits Syst II 2020;67(5):936–40. http://dx.doi.org/10.1109/TCSII.2020.2980988.

[24] Zong H, Zhang C, Lyu J, Cai X, Molinas M, Rao F. Generalized MIMO sequence impedance modeling and stability analysis of MMC-HVDC with wind farm considering frequency couplings. IEEE Access 2020;8:55602–18. http://dx.doi.org/10.1109/ACCESS.2020.2981177.

[25] del Giudice D, Brambilla A, Linaro D, Bizzarri F. Modular multilevel converter impedance computation based on periodic small-signal analysis and vector fitting. IEEE Trans Circuits Syst I Regul Pap 2022;1–11. http://dx.doi.org/10.1109/TCSI.2021.3138515.

[26] Yazdani A, Iravani R. A unified dynamic model and control for the voltage-sourced converter under unbalanced grid conditions. IEEE Trans Power Deliv 2006;21(3):1620–9. http://dx.doi.org/10.1109/TPWRD.2006.874641.

[27] B4-57 CW. Guide for the development of models for HVDC converters in a HVDC grid. CIGRÉ (WG Brochure); 2014.

[28] Kundur P. Power system stability and control. New York: McGraw-Hill; 1994.

[29] Tu Q, Xu Z, Xu L. Reduced switching-frequency modulation and circulating current suppression for modular multilevel converters. IEEE Trans Power Deliv 2011;26(3):2009–17.

[30] Song G, Wang T, Huang X, Zhang C. An improved averaged value model of MMC-HVDC for power system faults simulation. Int J Electr Power Energy Syst 2019;110:223–31. http://dx.doi.org/10.1016/j.ijepes.2019.03.016, URL: https://www.sciencedirect.com/science/article/pii/S0142061518313905.

[31] Aprille TJ, Trick T. Steady-state analysis of nonlinear circuits with periodic inputs. Proc IEEE 1972;60(1):108–14.

[32] Parker TS, Chua LO. Practical numerical algorithms for chaotic systems. New York: Springer-Verlag; 1989.

[33] Ascher UM, Petzold LR. Computer methods for ordinary differential equations and differential-algebraic equations, vol. 61. SIAM; 1998.

[34] Chua L, Desoer CA, Kuh ES. Linear and nonlinear circuits. New York: McGraw-Hill Editions; 1987.

[35] Vlach J, Singhal K. Computer methods for circuit analysis and design. Van Nostrand Reinhold Company; 1983.

[36] Shah S, Koralewicz P, Gevorgian V, Liu H, Fu J. Impedance methods for analyzing stability impacts of inverter-based resources: Stability analysis tools for modern power systems. IEEE Electrif Mag 2021;9(1). http://dx.doi.org/10.1109/mele.2020.3047166.

[37] Shah S, Koralewicz P, Gevorgian V, Wallen R, Jha K, Mashtare D, Burra R, Parsa L. Large-signal impedance-based modeling and mitigation of resonance of converter-grid systems. IEEE Trans Sustain Energy 2019;10(3):1439–49. http://dx.doi.org/10.1109/TSTE.2019.2903478.

[38] Di Bernardo M, Budd C, Champneys A, Kowalczyk P. Piecewise-smooth dynamical systems, theory and applications. London: Springer-Verlag; 2008.

[39] Bizzarri F, Brambilla A, Storti Gajani G. Steady state computation and noise analysis of analog mixed signal circuits. IEEE Trans Circuits Syst I Regul Pap 2012;59(3):541–54. http://dx.doi.org/10.1109/TCSI.2011.2167273.

[40] Telichevesky R, Kundert K, J. W. Efficient AC and noise analysis of two-tone RF circuits. In: DAC. 1996, p. 292–7.

[41] Zadeh L. Frequency analysis of variable networks. Proc IRE 1950;38(3):291–9. http://dx.doi.org/10.1109/JRPROC.1950.231083.

[42] Bakhshizadeh MK, Blaabjerg F, Hjerrild J, Wang X, Kocewiak L, Bak CL. A numerical matrix-based method for stability and power quality studies based on harmonic transfer functions. IEEE J Emerg Sel Top Power Electron 2017;5(4):1542–52. http://dx.doi.org/10.1109/JESTPE.2017.2742241.

[43] Araújo A, Tonidandel D. Steinmetz and the concept of phasor: A forgotten story. J Control, Autom Electr Syst 2013;24(3):388–95.

[44] Ramos PM, Janeiro FM. Vector fitting based automatic circuit identification. In: 2016 IEEE International Instrumentation and Measurement Technology Conference Proceedings. 2016, p. 1–6. http://dx.doi.org/10.1109/I2MTC.2016.7520553.

[45] Beerten J, D'Arco S, Suul JA. Frequency-dependent cable modelling for small-signal stability analysis of VSC-HVDC systems. IET Gener, Transm Distrib 2016;10(6):1370–81.

[46] Ji K, Pang H, Yang J, Tang G. Dc side harmonic resonance analysis of MMC-HVDC considering wind farm integration. IEEE Trans Power Deliv 2020;1.

[47] Emadi A, Khaligh A, Rivetta CH, Williamson GA. Constant power loads and negative impedance instability in automotive systems: definition, modeling, stability, and control of power electronic converters and motor drives. IEEE Trans Veh Technol 2006;55(4):1112–25.

[48] Wu H, Wang X, Kocewiak LH. Impedance-based stability analysis of voltage-controlled MMCs feeding linear AC systems. IEEE J Emerg Sel Top Power Electron 2020;8(4):4060–74. http://dx.doi.org/10.1109/JESTPE.2019.2911654.

[49] Gong Z, Zhao S, Wu X, Zheng C, Zhou J. A global fault current limiting strategy for the MMC-HVDC grid with a reduced DC reactor. Int J Electr Power Energy Syst 2022;140:108088. http://dx.doi.org/10.1016/j.ijepes.2022.108088, URL: https://www.sciencedirect.com/science/article/pii/S0142061522001302.

[50] Xiao L, Xu Z, Xiao H, Zhang Z, Wang G, Xu Y. Electro-mechanical transient modeling of MMC based multi-terminal HVDC system with DC faults considered. Int J Electr Power Energy Syst 2019;113:1002–13. http://dx.doi.org/10.1016/j.ijepes.2019.06.003, URL: https://www.sciencedirect.com/science/article/pii/S0142061518331831.

[51] Sun J, Liu H. Sequence impedance modeling of modular multilevel converters. IEEE J Emerg Sel Top Power Electron 2017;5(4):1427–43. http://dx.doi.org/10.1109/JESTPE.2017.2762408.